AGU PUBLICATIONS

JGR

Journal of Geophysical Research: Solid Earth

RESEARCH ARTICLE
10.1002/2016JB012895

Key Points:
- Thin-layer thickness measurements made from differences between time lapse seismic reflection surveys
- Inverse modeling of shallowest CO_2-filled layer at Sleipner Field to determine thickness
- Volume of CO_2 in shallowest layer increases quadratically with time

Supporting Information:
- Supporting Information S1

Correspondence to:
L. R. Cowton,
lrc37@cam.ac.uk

Citation:
Cowton, L. R., J. A. Neufeld, N. J. White, M. J. Bickle, J. C. White, and R. A. Chadwick (2016), An inverse method for estimating thickness and volume with time of a thin CO_2-filled layer at the Sleipner Field, North Sea, *J. Geophys. Res. Solid Earth*, *121*, 5068–5085, doi:10.1002/2016JB012895.

Received 5 FEB 2016
Accepted 19 JUN 2016
Accepted article online 24 JUN 2016
Published online 13 JUL 2016

©2016. American Geophysical Union. All Rights Reserved.

An inverse method for estimating thickness and volume with time of a thin CO_2-filled layer at the Sleipner Field, North Sea

L. R. Cowton[1], J. A. Neufeld[1,2,3], N. J. White[1], M. J. Bickle[1], J. C. White[4], and R. A. Chadwick[4]

[1]Bullard Laboratories, Department of Earth Sciences, University of Cambridge, Cambridge, UK, [2]BP Institute, University of Cambridge, Cambridge, UK, [3]Department of Applied Mathematics and Theoretical Physics, University of Cambridge, Cambridge, UK, [4]British Geological Survey, Keyworth, UK

Abstract Migration of CO_2 through storage reservoirs can be monitored using time lapse seismic reflection surveys. At the Sleipner Field, injected CO_2 is distributed throughout nine layers within the reservoir. These layers are too thin to be seismically resolvable by direct measurement of the separation between reflections from the top and bottom of each layer. Here we develop and apply an inverse method for measuring thickness changes of the shallowest layer. Our approach combines differences in traveltime down to a specific reflection together with amplitude measurements to determine layer thicknesses from time lapse surveys. A series of synthetic forward models were used to test the robustness of our inverse approach and to quantify uncertainties. In the absence of ambient noise, this approach can unambiguously resolve layer thickness. If a realistic ambient noise distribution is included, layer thicknesses of 1–6 m are accurately retrieved with an uncertainty of ±0.5 m. We used this approach to generate a thickness map of the shallowest layer. The fidelity of this result was tested using measurements of layer thickness determined from the 2010 broadband seismic survey. The calculated volume of CO_2 within the shallowest layer increases at a rate that is quadratic in time, despite an approximately constant injection rate into the base of the reservoir. This result is consistent with a diminished growth rate of the areal extent of underlying layers. Finally, the relationship between caprock topography and layer thickness is explored and potential migration pathways that charge this layer are identified.

1. Introduction

Large-scale field trials of CO_2 storage are yielding high-quality, geophysical and geochemical data sets that improve our ability to assess the long-term stability of sequestered CO_2. Conclusions drawn from predictive flow models of CO_2 migration through storage reservoirs are only reliable provided that the observations against which they are calibrated are trustworthy. The Sleipner storage project in the North Sea is an important site for studying CO_2 migration for two reasons (Figure 1a). First, CO_2 is being injected into a pristine, shallow, saline reservoir (Figure 1b). The pristine nature of the aquifer means that the growth of bright reflectivity on postinjection surveys is attributable to CO_2 injection alone. The shallow depth of burial means that horizontal and vertical resolution are optimized. Second, the project's marine setting enables high-quality time lapse seismic reflection surveys to be acquired at regular intervals. In these surveys, it is well documented that dense-phase CO_2 is progressively filling a series of nine sandstone layers within the Utsira Formation (Figure 1b) [*Arts et al.*, 2004; *Bickle et al.*, 2007; *Boait et al.*, 2012]. In contrast to other layers, the shallowest layer within the reservoir (i.e., Layer 9) has received significant attention. Its complex planform has been extensively studied since seismic reflections from this layer are unaffected by flow of CO_2 in deeper parts of the reservoir [e.g., *Chadwick et al.*, 2009; *White et al.*, 2013; *Kiær*, 2015].

Subdued topography of the structural trap beneath which CO_2 is ponding means that the CO_2-filled layers are very thin with extensive planforms. On most of the seismic surveys, the bulk of these layers are thinner than the one quarter wavelength limit of vertical resolution for seismic reflection images [*Widess*, 1973]. Consequently, it is generally difficult to directly measure layer thickness from the seismic reflection images which means that volumetric estimates as a function of time are poorly known. As a result, many studies have focused on measuring changes in the areal planform of each layer, which are readily observed. These measurements have been used to test analytical fluid dynamical models of CO_2 flow throughout the reservoir

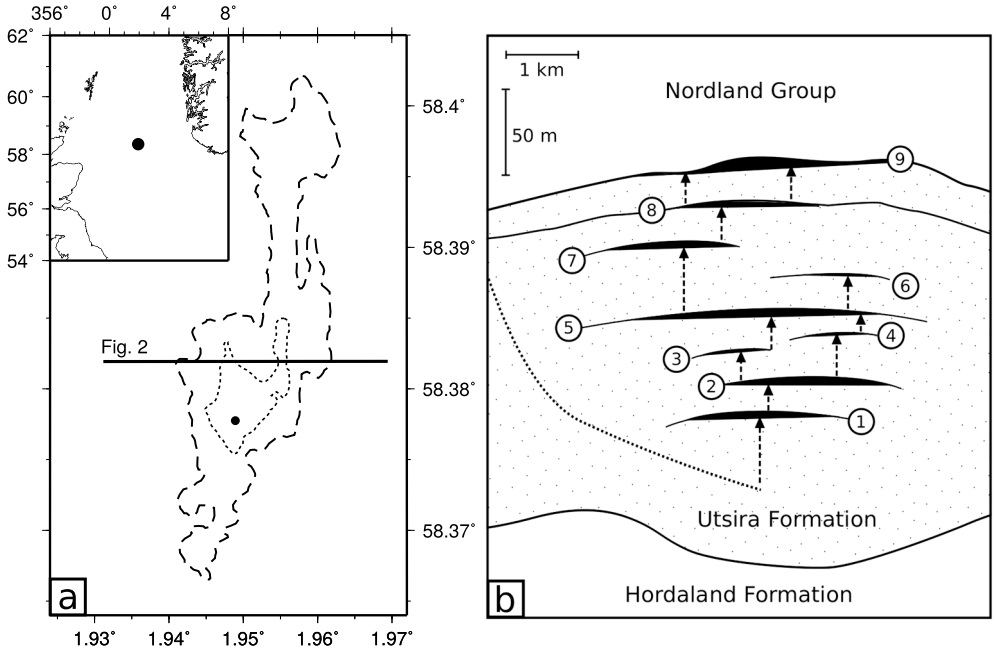

Figure 1. Location of Sleipner CO_2 project. (a) Map showing location and planform of injection reservoir. Dotted polygon = planform of CO_2-filled Layer 9 in 2002; dashed polygon = planform in 2010; solid circle = CO_2 injection point at base of reservoir; solid line = location of cross section shown in Figure 2. Inset map shows location of Sleipner project in North Sea. (b) Schematic diagram showing present day configuration of injected CO_2 within reservoir. Unit with dotted pattern = Utsira Sandstone Formation; numbered black layers = nine CO_2-filled sandstone horizons separated by thin mudstones; dotted line = injection well; vertical arrows = notional interlayer flow of CO_2. Note vertical exaggeration.

[*Bickle et al.*, 2007; *Boait et al.*, 2012]. More comprehensive, history-matching numerical reservoir simulations have been used to analyze the evolution of Layer 9 [*Chadwick and Noy*, 2010; *Cavanagh*, 2013; *Zhang et al.*, 2014]. In these numerical simulations, measurable parameters such as permeability, reservoir temperature, and caprock topography are adjusted in order to match the observed planform of the CO_2-filled layer. While these simulations do provide insight into the potential distribution of CO_2 within Layer 9, they have not yet been able to accurately match the observed planform of CO_2 on appropriate timescales.

Different approaches have been used to estimate the thickness of the CO_2-saturated sandstone at Layer 9 with varying degrees of success. Most of these techniques exploit amplitude or two-way traveltime pushdown measurements. For example, observed amplitudes of reflections have been used to measure thickness changes of Layer 9 [*Chadwick et al.*, 2005; *Kiær*, 2015]. Unfortunately, using amplitude information to measure layer thickness without calibration against a layer of known thickness necessitates assumptions about layer and wavelet properties with attendant uncertainties. *Williams and Chadwick* [2012] used spectral decomposition to resolve layer thickness but found that it is difficult to resolve thicknesses of less than ~4 m using this technique. *Furre et al.* [2015] used pushdown observations at the top of Layer 8 to estimate the thickness of the CO_2-saturated sandstone in Layer 9 required to produce this effect. However, this approach is complicated by the need to account for pull-up of the same reflection caused by interference effects.

Here we describe a general method for estimating the thickness of a thin, CO_2-filled layer trapped beneath a simple structure. This method simultaneously inverts multiple measurements of both amplitude and traveltime anomalies between different surveys for a given reflective horizon. We have tested it on synthetic data and then applied it to time lapse seismic surveys acquired between 1994 and 2010 at the Sleipner Field. Formal uncertainties are quantified using synthetic tests. Our approach builds upon previous attempts to constrain layer thickness using amplitude and traveltime measurements [*Kiær*, 2015; *Furre et al.*, 2015]. These results have been used to estimate the volume of CO_2 within Layer 9 as a function of time. In this way, a quantitative understanding of the spatial distribution of CO_2 together with its rate of migration through a saline storage reservoir can be obtained.

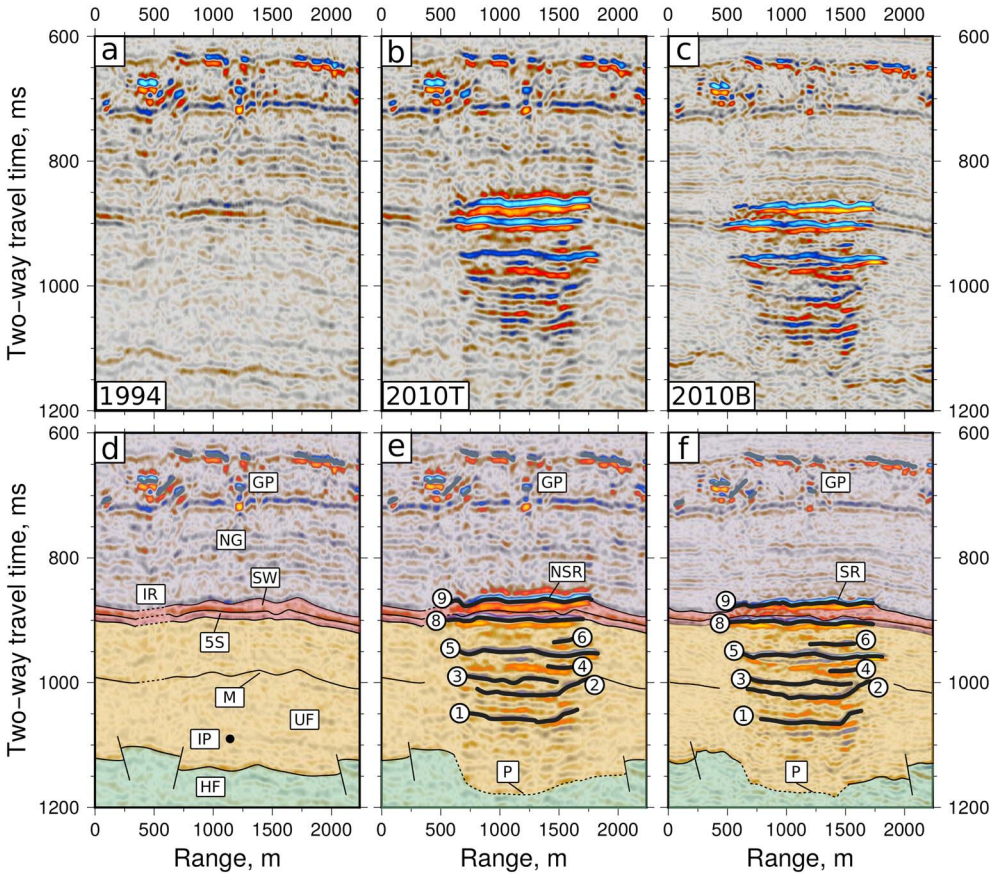

Figure 2. Time lapse seismic reflection surveys. (a–c) Single crossline from 1994 (i.e., preinjection), 2010, and 2010 (broadband) surveys. Red/blue reflections = positive/negative amplitudes. (d–f) Interpreted images. HF (green) = Hordaland Formation; UF (yellow) = Utsira Formation; NG (blue) = Nordland Group; SW (red) and 5S = Sand Wedge unit including 5 m thick shale horizon; encircled numbers = nine mappable layers; GP = pockets of natural gas; IP = projected CO_2 injection point; M = peg-leg multiple event; IR = incoherent reflections; P = pushdown of base Utsira Formation; NSR = unseparated reflection at Layer 9; SR = separated reflections at Layer 9.

2. Sleipner Carbon Dioxide Storage Project

Since 1996, subsurface injection of dense-phase CO_2 has been carried out at the Sleipner Field, which is located in the eastern part of the North Sea (Figure 1a). Natural gas extracted from the Sleipner West field contains up to 9.5% CO_2 by volume [*Baklid et al.*, 1996]. This CO_2 is extracted at the platform and reinjected into a pristine saline reservoir, the Utsira Formation, at a rate of ~1 Mt yr^{-1} [*Chadwick et al.*, 2009]. In the vicinity of the Sleipner Field, the Utsira Formation is up to 300 m thick and it is overlain by approximately 250 m of shale from the Nordland Group. The Utsira Formation is a highly porous and unconsolidated sandstone that is subdivided by ~1 m thick shale layers at intervals of about 30 m. These shale layers are too thin to be imaged by seismic reflection surveying and they are probably not laterally continuous between existing, widely spaced exploration wells [*Zweigel et al.*, 2004]. A single 6.5 m mudstone layer close to the top of the Utsira Formation (commonly referred to as the "5 m Shale") separates the main part of the Utsira Formation from the uppermost sandstone layer of the Utsira Formation, known as the "Sand Wedge" (Figure 2). The base of the Utsira Formation is affected by mud diapirism and polygonal faulting within the underlying Hordaland Formation [*Zweigel et al.*, 2004]. Faulting is not observed within the Utsira Formation above the injection region.

Seismic reflection imaging is the primary method for monitoring offshore CO_2 storage reservoirs [*Benson and Cole*, 2008]. At the Sleipner Project, time lapse (i.e., four dimensional) seismic reflection surveys have been shot nearly every other year since 1999, following a preinjection survey that was acquired in 1994 (Figure 2). Each time lapse survey has been processed with reference to, and by benchmarking against, the preinjection survey. This approach facilitates comparison between preinjection and postinjection surveys. Importantly,

deconvolution techniques were used to ensure that the reflected waves have zero phase (i.e., maximum amplitude of the wave coincides with the locus of impedance contrast in two-way traveltime). *Boait et al.* [2012] found that these zero-phase waves approximate Ricker wavelets. No residual oil or gas reside within the reservoir and so any changes in the reflectivity are directly attributable to the presence of CO_2.

The preinjection survey, along with many of the subsequent surveys, was shot with the primary objective of imaging the Sleipner East natural gas reservoir at a depth of ~2300 m [*Eiken et al.*, 2000; *Furre and Eiken*, 2014]. Thus, the frequency content of this survey is not optimal for imaging the target depth of the CO_2-filled reservoir (i.e., ~800 m). Frequency content of the time lapse surveys has been adjusted to match that of the preinjection survey. This adjustment has the effect of decreasing the vertical resolution of the time lapse surveys. To objectively assess differences between the time lapse surveys, *Furre and Eiken* [2014] calculated a normalized RMS value for each survey compared to the 1994 survey [*Kragh and Christie*, 2002]. These values generally lie between 52 and 62%, suggesting that this suite of time lapse surveys are appropriately comparable [*Cantillo*, 2012].

In 2010, a broadband seismic survey was acquired using a dual sensor streamer configuration which enables the ghost reflection from the sea surface to be removed. This survey is richer in high frequencies and has considerably better vertical resolution [*Furre and Eiken*, 2014]. The effects of an improved frequency content are obvious when this broadband survey is compared with its filtered equivalent (Figure 2).

3. Layer Thickness Measurements

We have extended the classic thin bed analysis of *Widess* [1973] and *Kallweit and Wood* [1982] by developing an inverse approach that exploits a set of observations from a suite of time lapse seismic surveys. These observations consist of a combination of amplitude and traveltime anomaly measurements from a reflective horizon with respect to the baseline, preinjection survey. Our goal is to constrain the thickness of a layer that cannot be directly measured as a result of interference effects since it is thinner than the nominal vertical resolution. First, a one-dimensional forward model is developed which calculates the amplitude and traveltime anomaly caused by constructive interference of waves reflected from the boundaries of a thin layer. Second, this forward model is used to develop and test an inverse model which uses amplitude and traveltime anomaly measurements to calculate layer thickness. Finally, we apply the inverse model to amplitude and traveltime anomaly observations taken from time lapse surveys of the Sleipner Field.

3.1. Forward Model

Consider a zero-phase Ricker wavelet, $\psi(t)$, the normalized amplitude of which is given by

$$\psi(t) = \left\{1 - 2[\pi f_p(t - t_1)]^2\right\} \exp\left\{-[\pi f_p(t - t_1)]^2\right\}, \quad (1)$$

where t is time, t_1 is the position of the peak of the wavelet in time, and f_p is the peak frequency of the wavelet [*Ryan*, 1994]. The shape of this wavelet depends only on its peak frequency. If a wavelet is reflected from a single boundary, the amplitude and sign of the reflected wavelet principally depends upon the acoustic impedance contrast at this boundary. If the wavelet is reflected from a layer with upper and lower boundaries, the amplitude, arrival time and shape of the reflected wavelet is strongly dependent upon layer thickness. A synthetic reflection experiment along a wedge-shaped layer illustrates how interference between the reflected wavelets from the lower and upper boundaries occurs when the layer is thin compared with the wavelet (Figure 3).

If a thin layer of low impedance is embedded within a medium with an otherwise uniformly high impedance, reflections from the upper and lower boundaries have opposite polarity (Figure 3). The resultant wavelet, $\chi(t)$, produced by interference, is given by

$$\chi(t) = A_1 \left\{\psi(t) + A_r\psi(t - \delta)\right\}, \quad (2)$$

where δ is separation of the upper and lower boundaries of the layer in two-way traveltime, A_1 and A_2 are the amplitudes of reflections from the upper and lower boundaries, and $A_r = A_2/A_1$ (Figure 4a). To aid comparison with other published estimates, we also convert δ into layer thickness, given by $(\delta v)/2$, where $v = 1428 \pm 95$ m s^{-1} is the acoustic velocity of seismic waves that travel through a uniformly saturated, CO_2-filled layer at the top of the Utsira Formation (section 3.3; Appendix A).

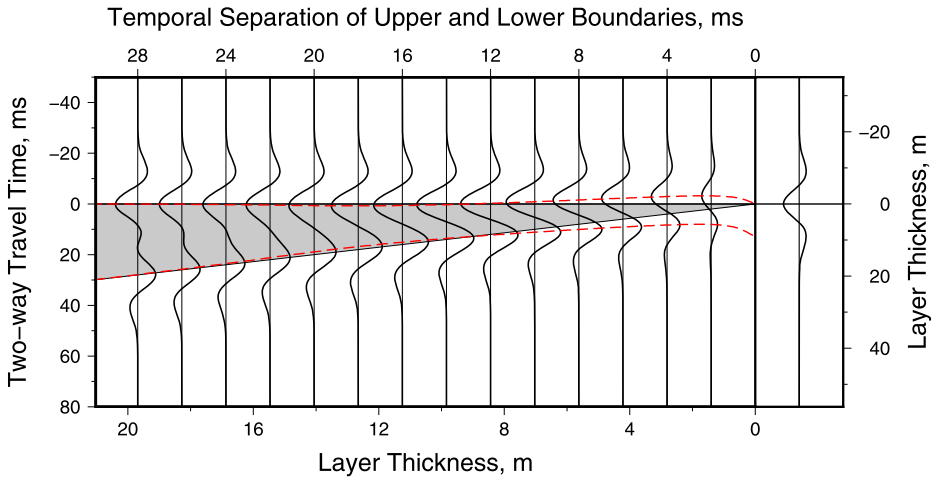

Figure 3. Seismic reflection modeling of wedge-shaped structure. Gray wedge = idealized CO_2 layer, for which lower boundary has impedance contrast that is 0.8 times that of upper boundary with opposite sign. Vertical wiggle to right of emboldened zero line = seismic trace calculated by convolving impedance contrast at single boundary with zero-phase Ricker wavelet; set of 14 vertical wiggles to left of zero line = seismic traces calculated for different wedge thicknesses; pair of red dashed lines = locus of peak-to-trough separation of each wavelet generated by interference. Note that velocity used to calculate thicknesses is 1428 m s^{-1}.

For thin layers, the effects of interference complicate straightforward correlation of the peak and trough of the resultant wavelet, $\chi(t)$, and boundaries of the layer cannot be visually resolved (Figure 3). If the thickness of the layer is equal to one quarter of the wavelength of the incident wavelet, separation of the peak and trough of $\chi(t)$ is approximately constant. This estimate yields the limit of vertical resolution for seismic reflection surveys (Figure 4b) [*Widess*, 1973].

Even though the effects of interference prevent direct calculation of layer thickness, there are two significant measurable effects. The best studied of these effects is tuning of the reflection from the upper boundary (Figure 4c). For thick layers where both boundaries are resolved, the amplitude of this reflection is constant. As the thickness of a layer decreases, the amplitude of the reflection increases, reaching its maximum value at the tuning thickness itself. Thus, tuning thickness is defined to be the thickness of a layer that produces maximum constructive interference between reflections from the lower and upper boundaries. For layers that are thinner than this tuning thickness, amplitude rapidly decreases toward the value expected for a reflection

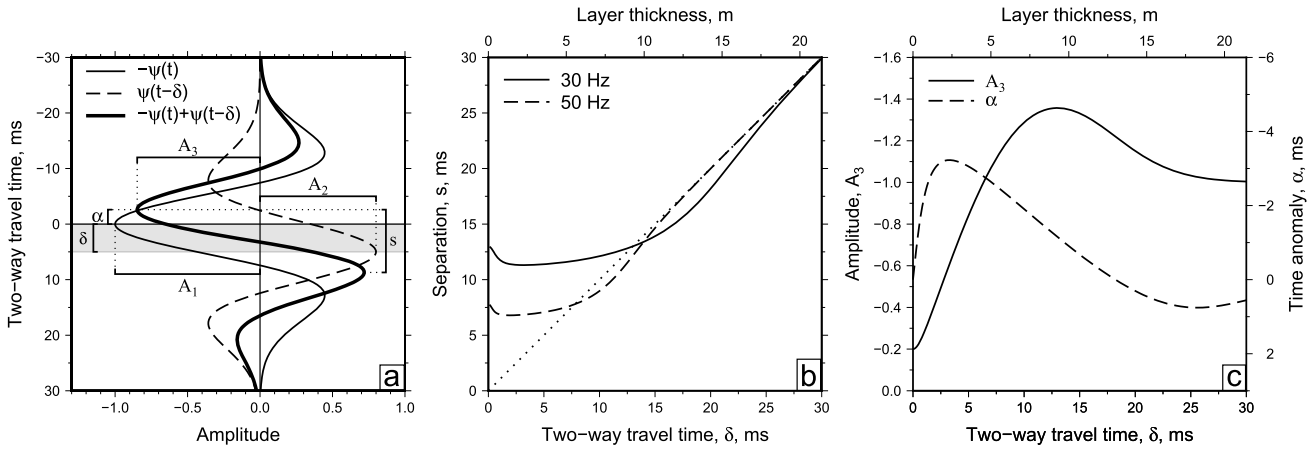

Figure 4. Separation, amplitude, and time anomaly as function of layer thickness for thin bed. (a) Amplitude as function of two-way traveltime. Thin wiggle = wave with amplitude A_1 reflected from top of thin bed; dashed wiggle = wave with amplitude A_2 reflected from base of thin bed ($A_2 = -0.8A_1$); bold wiggle = resultant wave with amplitude A_3 recorded at surface; δ-wide gray band = time delay across thin bed; α = traveltime anomaly between reflected wave from top of thin bed and resultant wave; s = separation between peak and trough of bold wiggle. (b) Separation, s, as function of time delay, δ, for two different frequencies. Solid line = 30 Hz; dashed line = 50 Hz; dotted line = 1:1 relationship. (c) Solid line = A_3 plotted as function of δ; dashed line = α plotted as function of δ. Note that velocity used to calculate thicknesses is 1428 m s^{-1}.

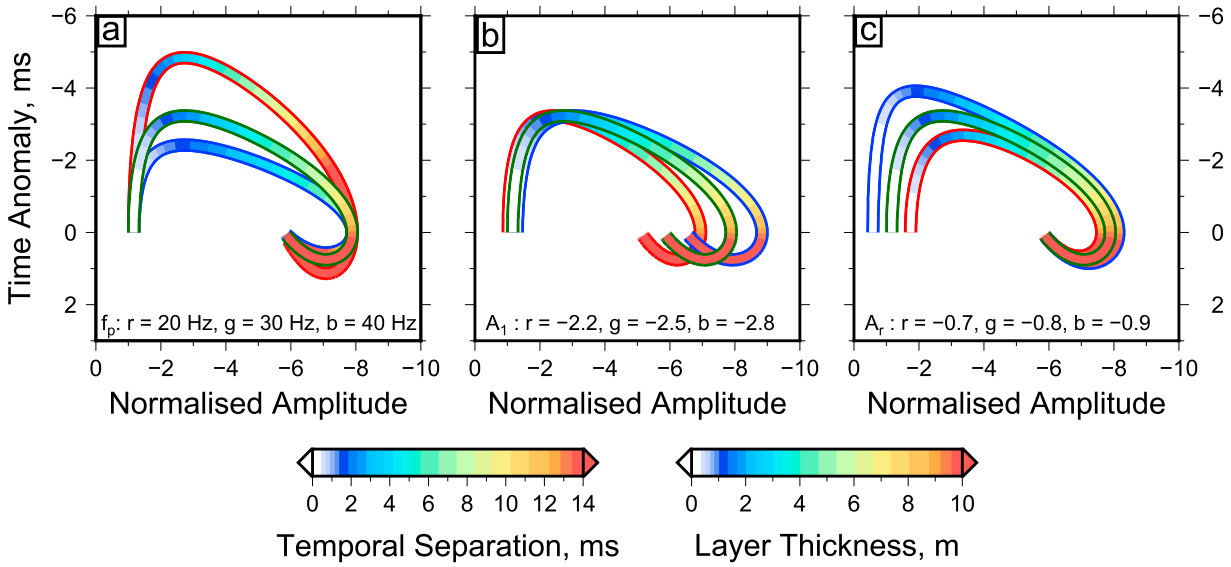

Figure 5. Relationships between amplitude, traveltime anomaly and layer thickness. (a) Change in time plotted as function of normalized (−10–0) amplitude for different frequencies, f_p, where $A_1 = -2.5$ and $A_r = -0.8$. Red outline = 20 Hz; green outline = 30 Hz; and blue outline = 40 Hz. (b) Same for different values of A_1 where $f_p = 30$ Hz and $A_r = -0.8$. Red outline = −2.2; green outline = −2.5; and blue outline = −2.8. (c) Same for different values of A_r, where $A_1 = -2.5$ and $f_p = 30$ Hz. Red outline = −0.7; green outline = −0.8; and blue outline = −0.9. Color scales refer to separation of upper and lower boundaries in milliseconds and to layer thickness in meters, using a velocity of 1428 m s^{-1}.

from a single boundary without the presence of a low impedance layer. In this way, the thickness of a thin layer can be estimated by measuring the amplitude of the reflected wavelet.

There are, however, two important drawbacks. First, it is difficult to calibrate the relationship between amplitude and layer thickness without information about a layer of known thickness. Without this information, the values of A_1 and A_r must be assumed. Second, amplitude does not monotonically increase with layer thickness, which introduces a fundamental ambiguity in the vicinity of the tuning thickness since two different values of layer thickness are consistent with a given value of amplitude [*Kallweit and Wood*, 1982].

The other measurable effect is the small traveltime anomaly for a wavelet reflected from the upper boundary (i.e., upper red dashed line shown in Figure 3) [*Furre et al.*, 2015]. This anomaly is generated by interference of reflections from the upper and lower boundaries of a layer. It is ~3 ms for a wavelet with a peak frequency, $f_p = 30$ Hz (Figure 4c). This value increases as frequency decreases and is particularly sensitive to very thin layers. While the anomaly is small, it is measurable, although the ability to identify it is susceptible to ambient and systematic noise. It also suffers from the same form of ambiguity since two different values of layer thickness are consistent with a given time anomaly.

By combining amplitude and traveltime anomaly measurements, an amplitude-thickness relationship can be calibrated without requiring a layer of known thickness. In this way, both forms of ambiguity can be reduced. In Figures 5a–5c, the traveltime anomaly, α, is plotted as a function of normalized amplitude for different values of other parameters. In each case, layer thickness varies along a unique curve, the precise shape of which depends upon f_p, the peak frequency of the reflected wavelet, A_1, the amplitude of the reflection from the upper boundary, and A_r, the ratio of the amplitudes of reflections from the upper and lower boundaries. Distance along a given curve is a function of the temporal separation between reflections from the upper and lower boundaries of the layer. The value of this separation is converted into thickness using $v_{CO_2} = 1428$ m s^{-1} (Appendix A).

It is clear that a combination of amplitude and traveltime anomaly measurements greatly reduces but does not entirely resolve the problem of ambiguity. In practice, both measurements are subject to degrees of uncertainty which will be dependent upon the quality of the seismic reflection survey. Furthermore, positive and negative trade-offs arise when f_p, A_1, and A_r are varied. In order to explore these issues, it is useful to carry out tests by inverting a synthetic data set which was generated by forward modeling.

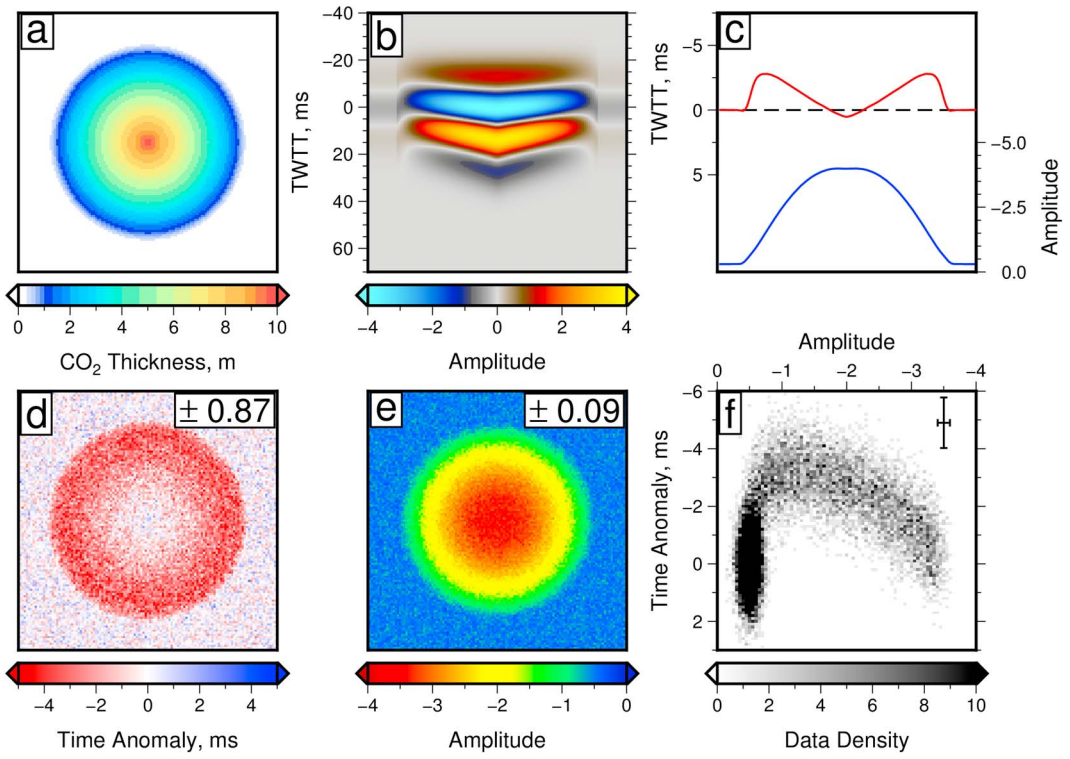

Figure 6. Forward model. (a) Circular patch of CO_2-filled layer (10 m thick at center). (b) Synthetic vertical seismic image through center of patch. (c) Details of seismic image showing traveltime anomaly (red) and reflection amplitude (blue). (d) Traveltime anomaly for region of patch with added random noise chosen from normal distribution with standard deviation of ±0.87 ms. (e) Reflection amplitude for region of patch with added random noise chosen from normal distribution with standard deviation of ±0.09. (f) Density plot of traveltime anomaly as function of amplitude (error bars indicative of uncertainties).

Consider a disk of CO_2-filled reservoir rock with arbitrary dimensions, for which thickness varies as a function of radius (Figure 6a). First, we calculate the seismic image of this disk where $f_p = 30$ Hz, $A_1 = -2.5$, and $A_r = -0.8$ (Figures 6b and 6c). Second, traveltime anomalies, α, and amplitudes, A_3, across the disk are calculated by assuming that ambient noise is normally distributed with standard deviations of ±0.87 ms and ±0.09, respectively (Figures 6d and 6e). Levels of ambient noise were chosen to match those encountered in time lapse seismic surveys from the Sleipner Field. Finally, α is plotted as a function of A_3 to reveal the expected trend (Figure 6f).

3.2. Inverse Model

The challenge is to use this distribution of synthetic measurements and their associated uncertainties to estimate the radial variation of thickness across the original disk. Since there are only three independent parameters, (i.e., f_p, A_1, A_r), a pragmatic method for solving this inverse problem is by parameter sweep. Traveltime anomaly and amplitude measurements are scaled by their respective uncertainties and a misfit function, M, is defined as a measure of the difference between the observed variation of α with A_3 and a calculated model (Figure 7a). Here M is given by

$$M = \frac{1}{N}\sum\sqrt{\left(\frac{A_3^o - A_3^c}{\sigma_{A_3}}\right)^2 + \left(\frac{\alpha^o - \alpha^c}{\sigma_\alpha}\right)^2}, \tag{3}$$

where N is the number of data points, A_3^o and α^o are the observed amplitude and traveltime anomaly measurements, A_3^c and α^c are their calculated values, and σ_{A_3} and σ_α are independent uncertainties. The variation of M as a function of f_p, A_1 and A_r is shown in three orthogonal slices (Figures 7b–7d). These slices demonstrate that A_1 and A_r trade off positively against each other and that the value of f_p does not significantly affect M.

Once the global minimum of the misfit function has been identified by parameter sweep, the way in which layer thickness varies as a function of α and A_3 can be determined (Figure 7e). Note that the maximum value

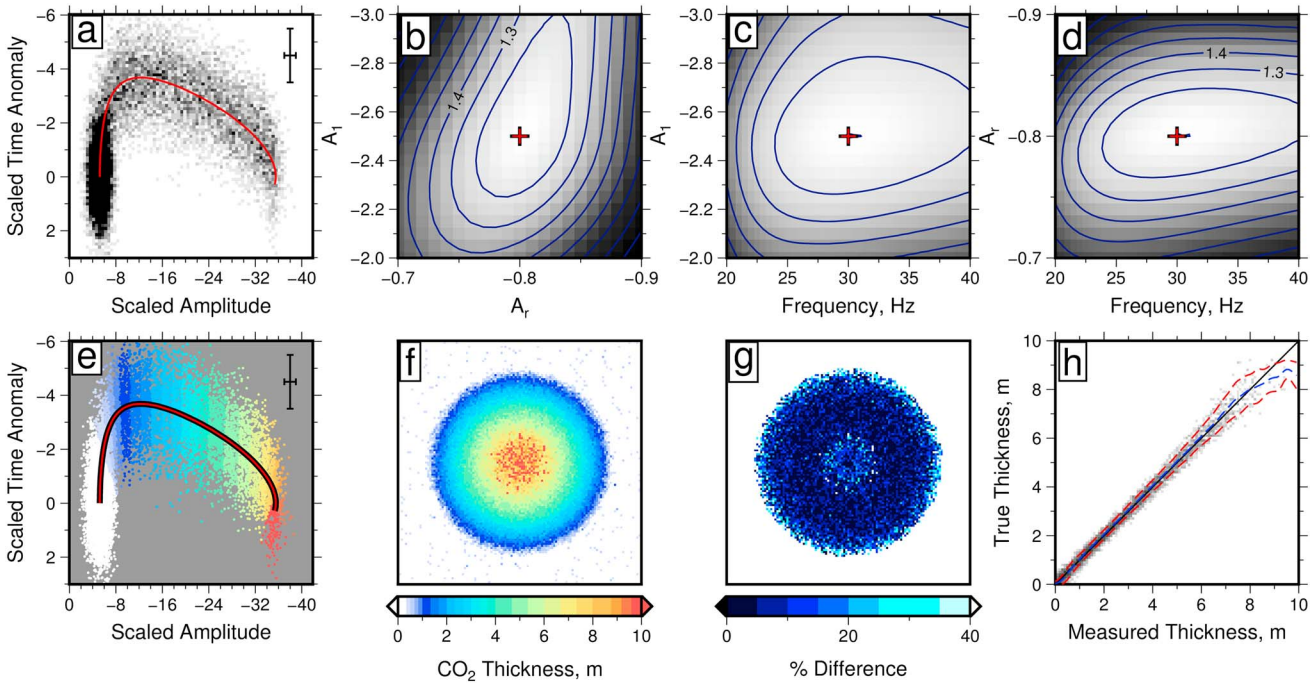

Figure 7. Inverse model. (a) Density plot of traveltime anomaly as function of amplitude scaled by their respective uncertainties (error bars indicative of uncertainties). Red line = best fit model for $A_r = -0.8$, $A_1 = -2.5$, and $f_p = 30$ Hz. (b–d) Orthogonal slices through misfit function. Red cross = global minimum where $A_r = -0.8$, $A_1 = -2.5$, and $f_p = 30$ Hz. (e) Same as Figure 7a where color scale indicates measured layer thickness. Black line = relationship used to generate forward model; red line = best fit relationship determined by parameter sweep of misfit function. (f) Thickness of CO_2-filled layer for region of patch determined using inverse model. (g) Percentage difference between recovered and actual thickness. (h) Plot of actual against recovered thickness. Black line = 1:1 relationship; blue line = mean true thickness for each measured thickness; pair of red dashed lines = 1 standard deviation.

of layer thickness can be fixed in order to improve the fit when ambient noise levels are high. In this synthetic test, a maximum value of 10 m was chosen. It was found by iteratively fitting the observations until a calculated distribution was identified that honors the distribution of observations without the risk of overestimating thickness values. Limiting the maximum measurable thickness in this way means that in some regions thickness could be underestimated. A significant advantage is that it sidesteps any remaining ambiguity in the vicinity of the tuning thickness when ambient noise levels are high.

Our synthetic test shows that inverse modeling can successfully retrieve the original values of f_p, A_1, and A_r. These values can then be used to recover the original distribution of layer thicknesses (Figures 7e and 7f). In practice, the best fitting model is used to translate individual measurements of both amplitude, A_3, and traveltime anomaly, α, into layer thicknesses which can be spatially plotted. In the complete absence of ambient noise, this translation is accurate and recovery of layer thicknesses is perfect, even for thicknesses that exceed the tuning thickness (Figures S1 and S2 in the supporting information.). If realistic levels of ambient noise are included, the difference between the original and recovered disks is small (Figures 7g and 7h). Including uncertainties in the velocity of seismic waves through CO_2-saturated sandstone, our results suggest that calculated thicknesses have an uncertainty of ± 0.5 m between 1 m and 6 m. Above 6 m, this uncertainty increases since values of A_3 and α become less sensitive to layer thickness (Figure 5). The problem of limiting the maximum measurable thickness is evident for the largest values where the correlation between observed and calculated values is not as good (Figure 7h). Additional synthetic tests were carried out using different levels of ambient noise for 16 m thick layers (Figures S3–S6 in the supporting information). These tests demonstrate that large thicknesses can be reliably recovered in the presence of noise. With increasing levels of ambient noise, the ability to recover layer thickness gradually deteriorates (Figure S6 in the supporting information).

3.3. Application

We have applied this inverse modeling strategy to a series of time lapse seismic surveys from the Sleipner Field. To obtain meaningful results, it is important to ensure that amplitudes of seismic waves on these different poststack surveys are comparable. In each case, amplitudes have been corrected for spherical divergence

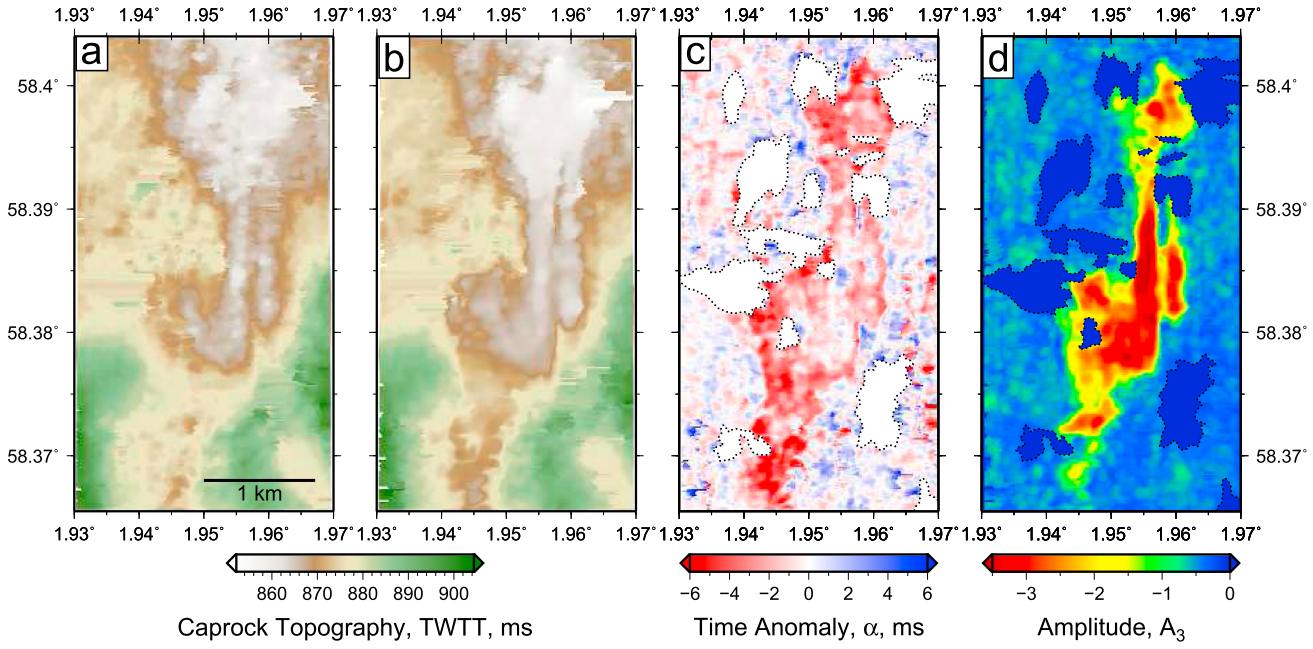

Figure 8. Comparative analysis of 1994 and 2010 surveys. (a) Two-way traveltime map of reflective boundary between reservoir and caprock for 1994 (i.e., preinjection) survey. (b) Same for 2010 survey. (c) Map of traveltime anomaly for reflective boundary between reservoir and caprock between 1994 and 2010 surveys. White polygons = locations where reflections are incoherent due to natural gas pockets in the overburden. (d) Map of amplitude of reflective boundary between reservoir and caprock for 2010 survey. Blue polygons = locations where reflections are incoherent.

of wavefronts as they propagate through the subsurface. Amplitudes have also been corrected for fold of cover (i.e., low-fold and high-fold seismic arrivals have the same amplitude). Finally, amplitudes have not been scaled or normalized. In general, each postinjection survey was processed in conjunction with the preinjection survey to ensure that preinjection and postinjection surveys are comparable. Initially, the 1994 preinjection and the 2010 time lapse surveys were compared. Mapping of both surveys shows that, where CO_2 is present, traveltime to the caprock-reservoir contact can be accurately identified and its relative change measured (Figure 8).

There are two important steps in our analysis. In the first step, traveltime anomaly and amplitude measurements are determined. Traveltime anomalies are measured by mapping the shape of the contact between the caprock and the top of the reservoir (i.e., the boundary between the Nordland Group and the Utsira Formation) on the 1994 (i.e., preinjection) and 2010 surveys (Figures 8a and 8b). Both horizons are smoothed using a symmetric nearest-neighbor filter that removes ambient noise while preserving sharp gradients at the edges of the CO_2 plume [*Hall*, 2007]. Figure 8c shows the traveltime difference between these two surveys. A systematic shallowing of the reflective boundary occurs where CO_2 is present in the 2010 survey. In the region surrounding the CO_2 plume, there should be no difference between surveys aside from minor variations in seismic acquisition and processing strategies. Small differences do occur which suggests that random noise is present. Analysis of this surrounding region shows that this noise follows an approximately normal distribution with a standard deviation of ~0.9 ms.

Spatial variation of the amplitude of this reflective boundary is extracted from the 2010 survey (Figure 8d). In the region surrounding the CO_2 plume, the range of values is normally distributed with a standard deviation of 0.09 and probably arises from a combination of measurement uncertainty and minor differences in acquisition and processing strategies. Crucially, uncertainties in traveltime anomaly and amplitude measurements do not covary. Traveltime anomaly is plotted as a function of amplitude and scaled by their respective uncertainties (Figure 9a).

In the second step, traveltime anomaly and amplitude measurements are fitted using a parameter sweep of f_p-A_1-A_r space (Figure 9). A global minimum is found at f_p =31 Hz, A_1 = −2.6, and A_r = −0.83. The value of f_p is consistent with an estimated frequency content of 30 Hz for the 2010 seismic survey [*Furre and Eiken*, 2014].

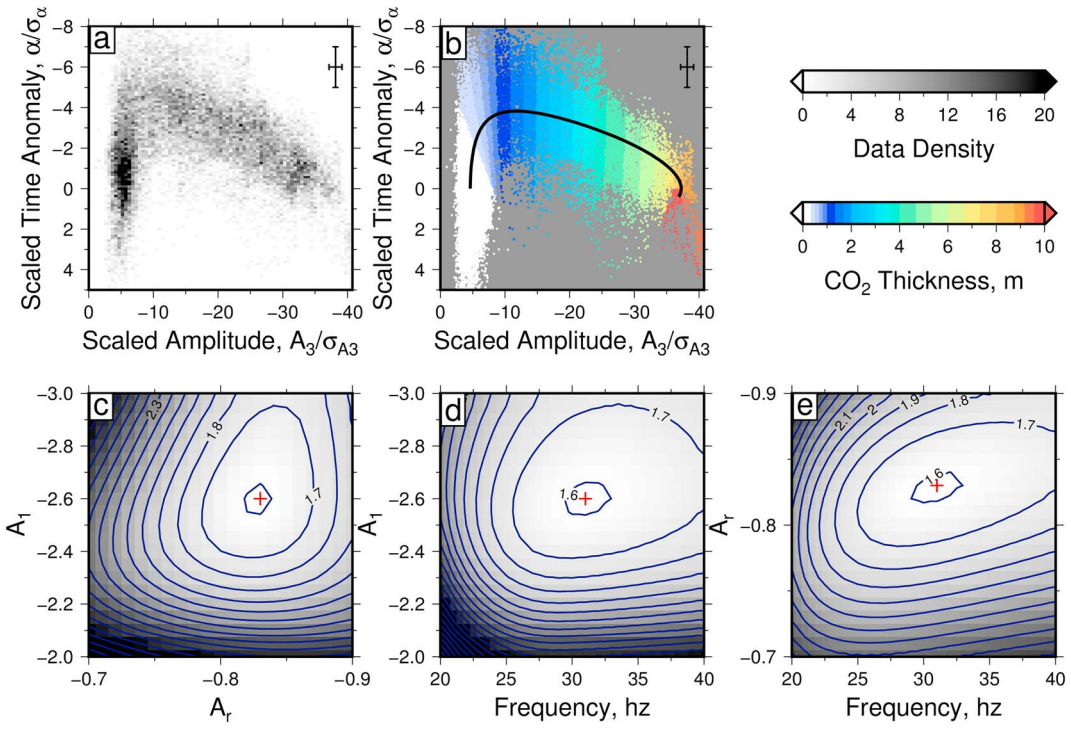

Figure 9. Data modeling. (a) Density plot of traveltime anomaly as function of amplitude for 2010 survey (each scaled by relative uncertainties). (b) Same as Figure 9a where color scale indicates layer thickness. Black line = best fit model at global minimum of misfit function. (c–e) Orthogonal slices through misfit function used to identify optimal values of A_r, A_1, and f_p. Red crosses = locus of global minimum found by grid search, where $A_r = -0.83$, $A_1 = -2.6$, and $f_p = 31$Hz.

Calculated values of δ are converted into thicknesses using the estimated acoustic velocity of CO_2-saturated sandstone, v_{CO_2}.

The acoustic velocity of CO_2-saturated sandstone within Layer 9 has been estimated in many different studies, but it is still debated. Since no empirical data exist for the Utsira Formation within the injection region, acoustic velocity is either calculated from rock physics estimates or from pushdown (i.e., time delay) of underlying reflections.

One important consideration is whether or not CO_2 saturation within the reservoir rock is uniform or patchy. If saturation is uniform, then acoustic velocity can be described using the Gassmann model. However, if saturation is patchy, then lateral dispersion and attenuation of seismic waves can occur and acoustic velocity may vary approximately linearly between end-members [*Rubino et al.*, 2011; *Williams and Chadwick*, 2012]. Attempts to match total pushdown of the base of the Utsira Formation due to the presence of CO_2 suggest that CO_2 is distributed in highly saturated thin layers between which regions with more diffuse, and possibly patchy, saturation occur [*Chadwick et al.*, 2005; *Boait et al.*, 2012]. This inference is supported by laboratory centrifuge experiments on core material from the Utsira Formation, which suggest that CO_2 saturation within each thin layer is likely to be very high with a thin capillary fringe along its base [*Chadwick et al.*, 2005]. *Rubino et al.* [2011] found that the effect of patchy saturation on acoustic velocity increased when saturation was low. They also concluded that wave-induced flow effects can be neglected when the thin, highly saturated layers within the Sleipner Field are considered. For these reasons, we have not incorporated the effects of patchy saturation on acoustic velocity in this analysis. If present, patchy saturation would cause a small increase in the calculated layer thickness. Variations in pore fluid pressure triggered by CO_2 injection could also affect the acoustic velocity of CO_2 itself. However, although pore fluid pressure variations have been inferred from temporal changes in amplitude signals at the Snøvit CO_2 injection site, no such changes have been observed within the Sleipner Field [*Eiken et al.*, 2011; *Chadwick et al.*, 2005].

Estimates of the acoustic velocity of a sandstone layer that is uniformly saturated with CO_2 lie between 1400 and 1500 m s^{-1} [e.g., *Arts et al.*, 2004; *Chadwick et al.*, 2005; *Ghaderi and Landrø*, 2009; *Williams and Chadwick*, 2012]. We note that there are two significant outliers [*Eiken et al.*, 2000; *Carcione et al.*, 2006]. Four alternative

estimates have been made using seismic observations: *Chadwick et al.* [2004] obtained a value of 1420 m s^{-1} based on the observed pushdown of reflective horizons beneath seismic chimneys; *Williams and Chadwick* [2012] calculated a velocity of 1478 m s^{-1} based on reflectivity of the upper boundary of Layer 9 by exploiting higher-resolution two-dimensional seismic profiles acquired in 2006; *Furre et al.* [2015] suggest that a velocity of 1400 m s^{-1} yields the optimal agreement between their thickness measurements and other studies; and finally *Chadwick et al.* [2016] measured a velocity of 1431 ± 62 m s^{-1} by correlating synthetic models with very small time shifts of reflections from the upper and lower boundaries of Layer 9 on the 2010 broadband survey. Here we used the Gassman model to obtain a value of 1428 ± 95 m s^{-1} for a CO_2 saturation of 0.8. The quoted uncertainty reflects the range of estimates found in the literature for different input parameters (Appendix A). This value embraces almost all of the estimates that are based on seismic observations, as well as those estimated from rock physics.

Finally, limiting the maximum measurable thickness to 10 m yields satisfactory results. For the 2010 survey, it is apparent that limiting the maximum thickness to 10 m has removed any potential ambiguity when solely converting amplitude measurements to thickness. It is important to emphasize that without using traveltime anomaly measurements in conjunction with amplitude measurements, an absence of ambiguity in amplitude values could not be discerned. The use of traveltime anomalies also permits accurate fitting of f_p, A_1, and A_r, improves resolution at the edge of the plume, and enables uncertainties to be gauged.

This limitation of 10 m is consistent with the maximum thickness found by direct measurement of the separation of reflections from the upper and lower boundaries of the CO_2-filled layer imaged on the 2010 (broadband) survey [*Furre and Eiken*, 2014]. The resultant distribution of thickness estimates shown in Figure 9b is then used to generate a planform map of CO_2-filled layer thickness.

3.4. Results

The same modeling procedure was applied to each of the six other seismic surveys that postdate the 1994 preinjection survey (Figure 10). Due to the modest planform areas and layer thicknesses, our inverse approach worked less well for the 1999, 2001, 2002 and 2004 surveys. For these particular surveys, the input parameter values obtained for the 2008 survey were used (i.e., $f_p = 30$ Hz, $A_1 = -2.6$, $A_r = -0.84$). This approximation does not significantly affect our principal conclusions. Calculated planform distributions show that the CO_2-filled layer thickens and grows along a north-south axis as a function of time. The spatial distribution of thicker patches of CO_2 is consistent between surveys and coheres with the shape of the caprock-reservoir contact. The CO_2-filled layer evidently thins toward the edge of the plume. This edge is accurately resolved since changes in traveltime are very sensitive to the thickness of a thin layer. Amplitude measurements alone are less sensitive to tapering edges of thin layers. Discontinuous regions are generally rare and mostly occur in later surveys when layer thicknesses exceed 6 m. Synthetic tests show that they are caused by greater degrees of uncertainty in the vicinity of the tuning thickness where thickness is more sensitive to minor changes in A_3 and α.

Our inverse modeling results were tested and benchmarked against the 2010 (broadband) seismic survey. This survey was acquired using dual-sensor streamers [*Furre and Eiken*, 2014]. This technique allows the receiver ghost to be accurately removed in the shot domain during signal processing. By removing periodic ghost notches, a significantly broader band spectrum of frequencies is achieved [*Furre and Eiken*, 2014]. The broadband survey has a peak frequency of 50 Hz which permits layers thicker than ~5.5 m to be measured directly using the separation of reflections from lower and upper boundaries of the CO_2-filled layer (Figure 4b). Mapping of the broadband survey shows that clear separation is mostly confined to the central portion of the CO_2-filled layer (Figure 11a). When the inverse modeling results and direct mapping are compared in this central portion, it is evident that inverse modeling yields slightly lower than expected thickness estimates (Figure 11c). Away from this central portion, comparative differences between the different approaches can be divided into two categories (Figures 11d and 11e). First, where thicknesses cannot be resolved by direct mapping, estimates can only be made using the inverse modeling results. Second, when thicknesses exceed ~6 m, synthetic tests show that the inverse modeling results are less reliable.

Our results compare favorably with previous attempts to constrain the thickness of Layer 9 at the Sleipner Field. Other studies that exploit amplitude measurements have yielded broadly similar results but none quantified the uncertainties [*Kiær*, 2015; *Chadwick et al.*, 2005]. Our results also imply that thickness maps generated using the observed pushdown of Layer 8 are excessively thick [*Furre et al.*, 2015]. This discrepancy could be

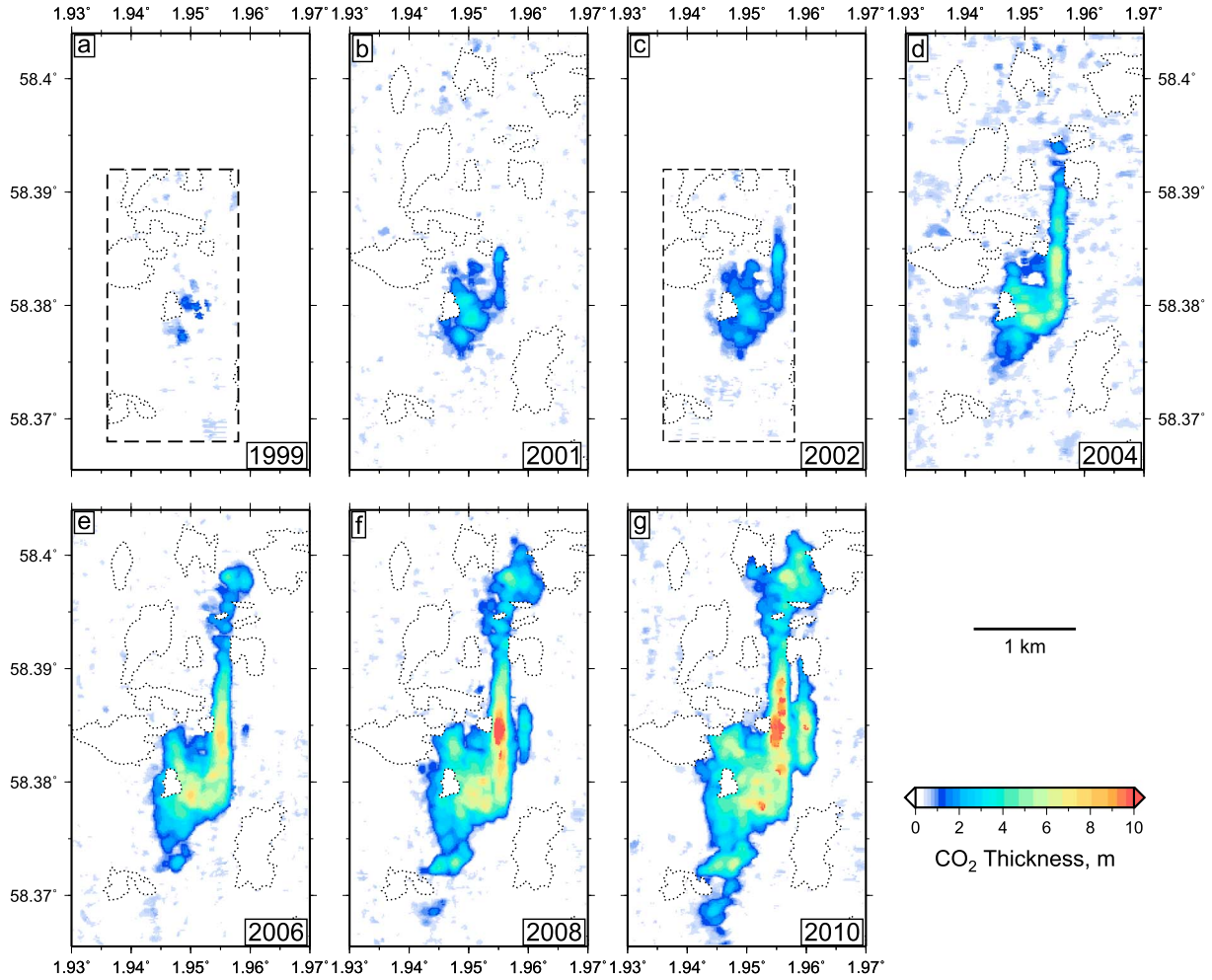

Figure 10. CO_2 distribution within Layer 9. Series of isopach maps showing CO_2 distribution within Layer 9 as function of calendar year from 1999 to 2010. White polygons = regions where reflections are incoherent due to natural gas pockets in the overburden; blue patches outside main CO_2 distribution are caused by ambient noise. Note that 1999 and 2002 surveys have smaller extent.

accounted for by including diffuse and patchy saturation of CO_2 between Layers 8 and 9, which would tend to increase pushdown without requiring a thickness change of the more highly saturated layer.

4. Fluid Dynamical Implications

4.1. Volumetric Estimates

The inverse modeling results were used to estimate the volume of CO_2 trapped within Layer 9 of the Utsira Formation as a function of time (Figure 12). We have assumed that the sandstone of Layer 9 has a porosity of 0.37 and a uniform saturation with CO_2 of 0.8 [*Arts et al.*, 2004; *Chadwick et al.*, 2004; *Bickle et al.*, 2007]. Uncertainty estimates were gauged by running synthetic models that replicate ambient noise levels within the different seismic surveys. The change in volume of Layer 9 increases with time and can be fitted using a function of the form

$$V = C\left(\frac{(t - t_0)}{\text{year}}\right)^n, \tag{4}$$

where V is volume of CO_2 in m^3, t is time in years, $C = 18{,}000 \pm 6000\ m^3$, $t_0 = 1998.9 \pm 0.2$ years, and $n = 1.9 \pm 0.1$. Our results are approximately consistent with a linearly increasing flux, $Q = (36{,}000 \pm 12{,}000)t\ m^3\ yr^{-1}$. We predict that the volume of CO_2 trapped inside Layer 9 by 2012 is approximately $2.4 \times 10^6\ m^3$. Equation (4) implies that dense-phase CO_2 took ~2.2 years to reach the top layer, following initiation of injection. Back-of-the-envelope calculations using a density of 690 kg m^{-3} suggest that about 12% of the total injected

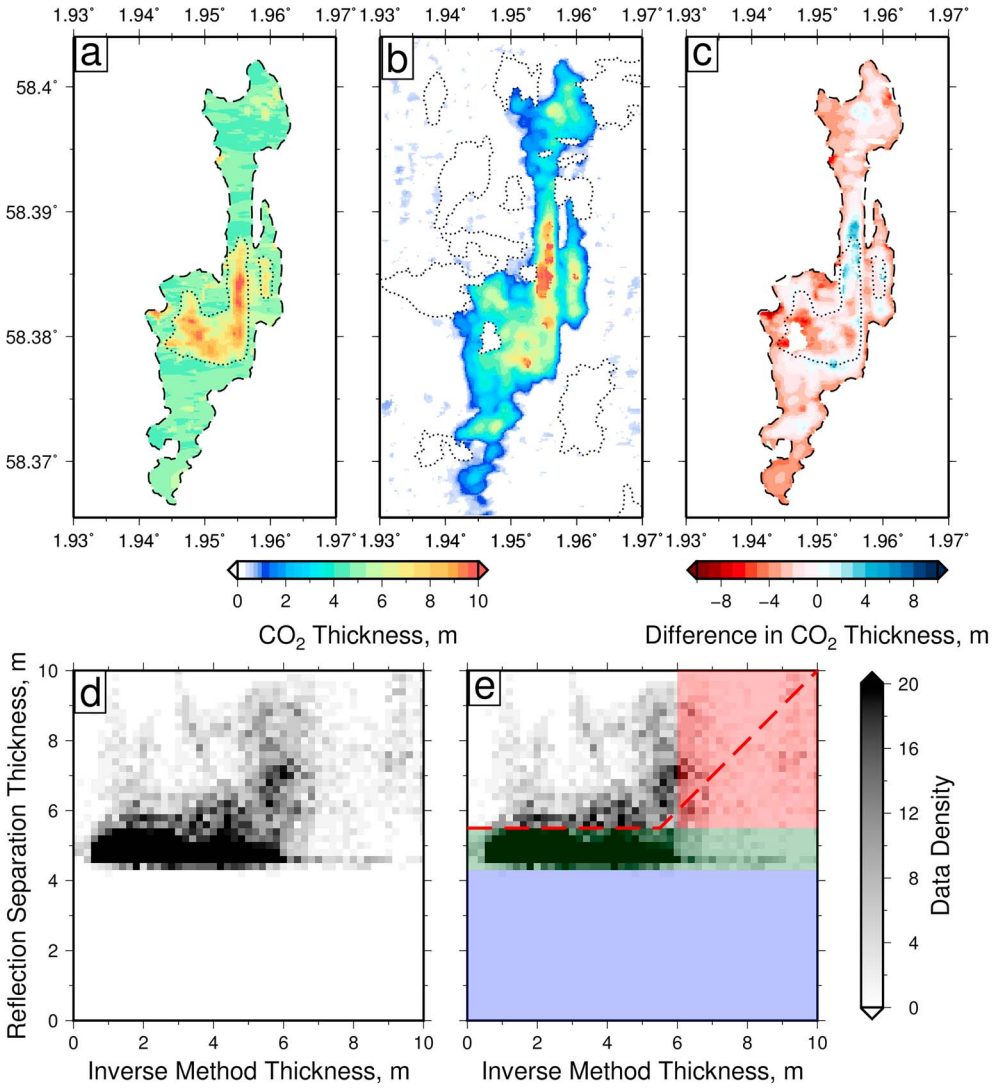

Figure 11. Comparison between inverse modeling and results of broadband survey. (a) Isopach map of CO_2 distribution within Layer 9 obtained using separation of reflective horizons on 2010 (broadband) survey. Dashed line = observed edge of amplitude anomaly; dotted line = region within which visible reflection separation occurs. (b) Isopach map of CO_2 distribution within Layer 9 obtained using inverse modeling. (c) Difference in measured thickness between Figures 11a and 11b. Dotted line = region within which visible reflection separation occurs. (d) Density plot showing comparison of thickness estimates based upon inverse modeling and upon broadband measurements. (e) Interpreted version of Figure 11d. Blue rectangle = region within which broadband measurements cannot resolve thickness; green band = limit of resolution for broadband measurements; red box = region within which larger uncertainties are expected for inverse modeling; red dashed line = expected trend for idealized case.

mass of CO_2 resided in Layer 9 by 2010 [*Williams and Chadwick*, 2012]. Between 2008 and 2010, an amount equivalent to approximately 25% of the injected CO_2 entered Layer 9.

CO_2 injection at the base of the Utsira Formation has been approximately constant since initiation of the Sleipner Project in 1996 [*Chadwick and Noy*, 2015]. Measurement of the areal extent of CO_2 trapped within each of the lower CO_2-filled layers suggests that some of these layers may have ceased growing [*Boait et al.*, 2012]. This observation suggests that the flux of CO_2 out of some layers is equal to that entering from below. New leakage pathways through the Utsira formation may be generated as a given layer expands, causing the leakage flux from a given layer to increase with time. These putative pathways could account for the proposed balance between input and leakage flux for lower layers. An important corollary is that the flux into upper layers should increase with time. Since there is no seismic evidence that CO_2 is migrating out of Layer 9, it is

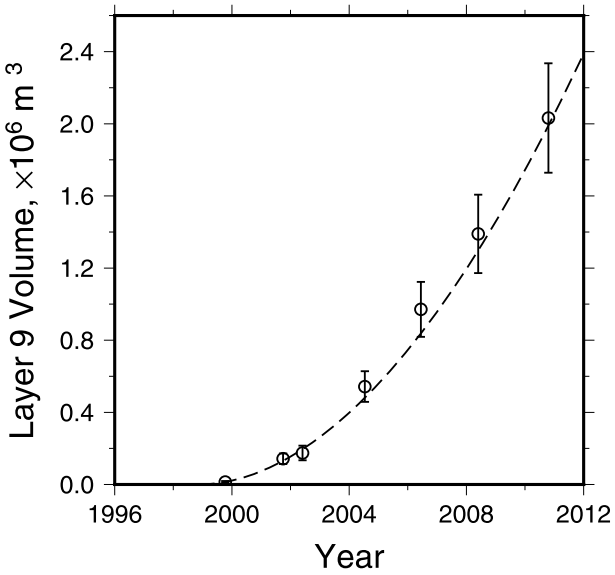

Figure 12. Volume estimates. Calculated volume of CO_2 based upon inverse modeling as function of calendar year for porosity of 0.37 and saturation of 0.8. Circles with error bars = estimates and their uncertainties; dashed line = best fitting relationship using $V = C\left(\frac{(t-t_0)}{\text{year}}\right)^n$ where C = 18,000 ± 6000 m^3, t_0 =1998.9 ± 0.2 years, and n =1.9 ± 0.1.

anticipated that the flux of CO_2 into this layer will continue to grow. These general inferences are consistent with modeling of CO_2 migration in layered strata [*Neufeld and Huppert*, 2009].

4.2. Topographic Controls and Migration Pathways

Topography of the caprock together with thickness of the CO_2-filled layer permit us to analyze the way in which flow of CO_2 responds to topographic relief. Figure 13a shows a cross section from the storage reservoir, which shows how Layer 9 has progressively filled. Uncertainty in converting traveltime to depth means the shape of the structural trap is not precisely known. Here topographic relief has been smoothed using a symmetric nearest neighbor filter. The bulk of the CO_2 is flowing buoyantly up slope and filling the dome-shaped trap. This observation suggests that topographic relief plays at least some role in controlling the shape of the top of the CO_2 plume. For the 1999 survey, the planform of CO_2 distribution suggests that a patch of CO_2 exists away from the main part of the dome-shaped trap. This isolated patch can be accounted for if CO_2 migrates vertically from a lower layer. This migration may have been facilitated by the presence of a prominent vertical chimney, SC1, on seismic profiles (Figures 13b and 13c). A smaller chimney, SC2, is visible farther up dip which may also have affected CO_2 flow to a lesser extent by generating an anomalously thick zone. Low-amplitude features such as these ones are usually interpreted to be near-vertical gas migration pathways [*Chadwick et al.*, 2004].

5. Conclusions

We present an inverse method for estimating the three-dimensional distribution of CO_2 within seismically imaged storage reservoirs as a function of time using a combination of traveltime anomaly and amplitude measurements. An important advantage of a combined approach is that a priori knowledge about impedance of the layer in question is not required. The validity and robustness of this method were carefully tested using forward and inverse modeling of synthetic data sets. In the absence of ambient noise, layer thickness can be resolved without ambiguity. For typically observed levels of ambient noise, it has been shown that the technique can resolve layer thicknesses in the range of 1–6 m with a vertical resolution of ±0.5 m.

We applied this method to the CO_2 storage reservoir at the Sleipner project. The planform of thickness variation for Layer 9 at the top of the reservoir was calculated. This planform was checked by comparing the 2010 time lapse and broadband surveys. In regions where a direct seismic measurement of layer thickness can be made, there is satisfactory agreement between both approaches within the bounds of uncertainty.

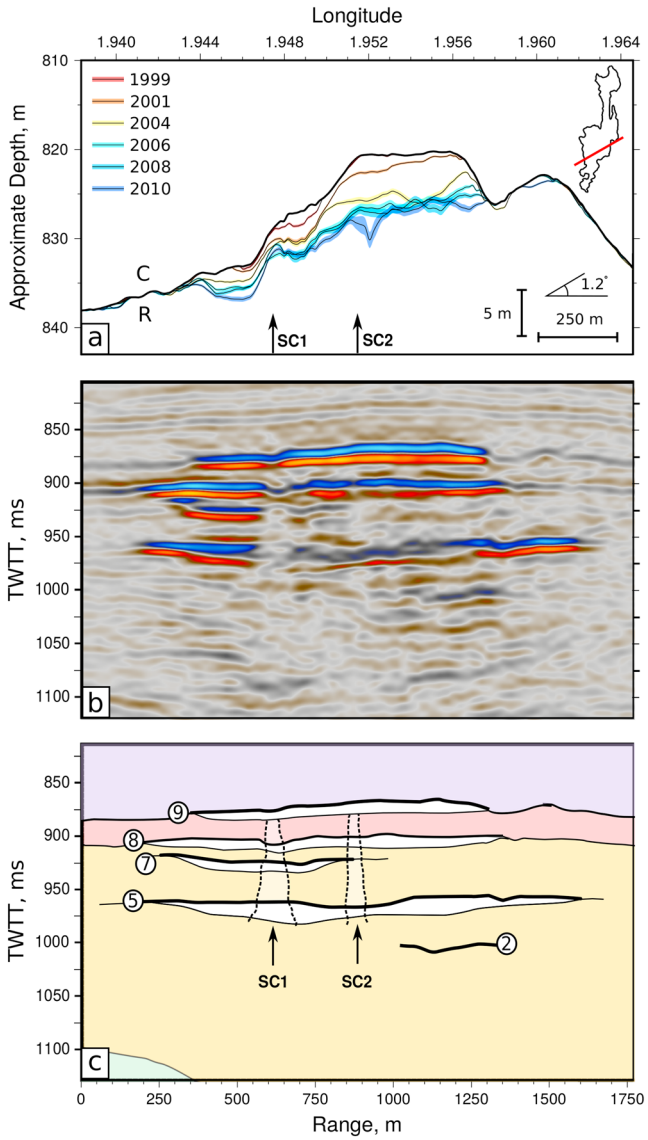

Figure 13. Vertically exaggerated cross section through Layer 9. (a) Colored lines = depth to base of Layer 9 through time where color and thickness indicate year of seismic survey acquisition and 1 standard deviation uncertainty, respectively (overburden velocity of 2150 m s^{-1} was assumed [*Zweigel et al.*, 2004]); black line = top of reservoir; vertical arrows = loci of possible seismic chimneys; C = caprock; R = reservoir; inset shows location of cross section. Note that 2002 survey is omitted for clarity. (b) Coincident seismic profile from 2010 (broadband survey). Red/blue = positive/negative amplitudes. (c) Interpretation of Figure 13b (see Figure 2 for color scheme). Numbered black lines capping white patches = selected CO_2-filled layers; vertical arrows = loci of possible seismic chimneys.

Our results can be used to calculate the volume of CO_2 within Layer 9 as a function of time. Volume increases with time at a growing rate, which suggests that CO_2 is migrating out of the lower part of the reservoir. Migration is probably facilitated by initiation of new pathways through intermediate shale layers or by changes in the flow capabilities of existing pathways. By comparing patterns of layer growth with appropriate cross sections from the 2010 broadband survey, we suggest that subvertical chimney structures might play a role in the upward migration of dense-phase CO_2. These thickness and volume estimates provide a new benchmark against which analytical and numerical fluid dynamical models can be tested.

Appendix A: Acoustic Velocity of CO_2-Saturated Rock

The Gassmann model is used to calculate the velocity of seismic waves that travel through a CO_2-saturated sandstone [*Mavko et al.*, 2009]. Uncertainties in the estimates of input parameters are used to determine upper and lower bounds.

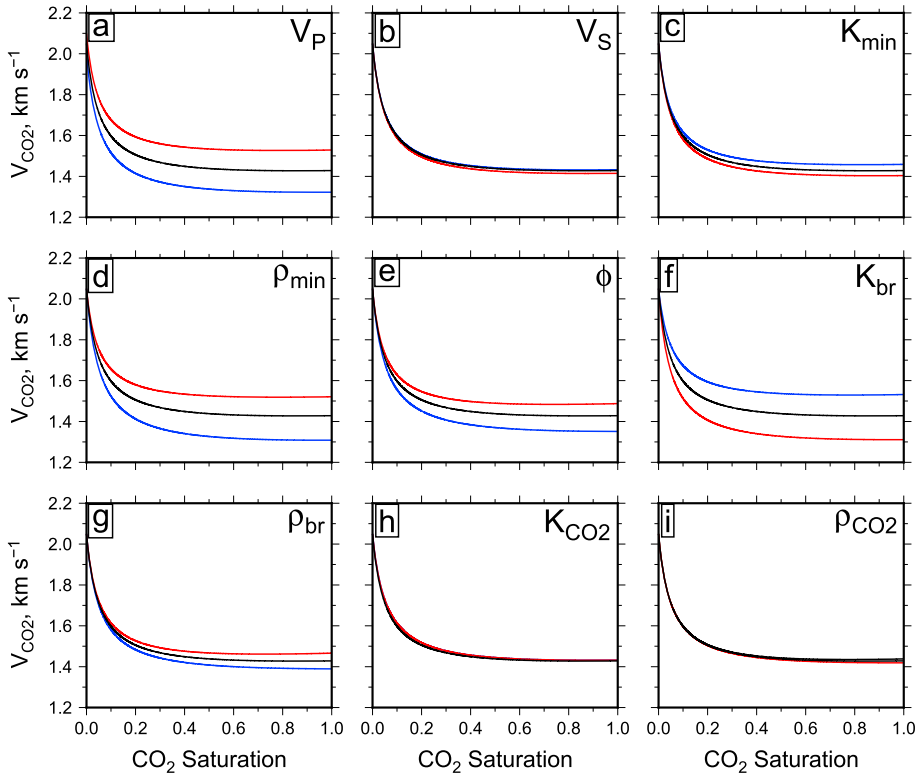

Figure A1. *P* wave velocity calculations showing sensitivity to input parameters. (a) Black line = *P* wave velocity as function of CO_2 saturation in water-saturated sandstone; red/blue lines = uncertainty range for input $v_P \pm 10\%$. (b) *S* wave velocity. (c) Bulk modulus of mineral material. (d) Density of mineral material. (e) Porosity. (f) Bulk modulus of ambient brine. (g) Density of ambient brine. (h) Bulk modulus of CO_2. (i) Density of CO_2.

Body wave velocities through a homogeneous, elastic, isotropic medium are given by

$$v_P = \left(\frac{K + \frac{4}{3}\mu}{\rho} \right)^{\frac{1}{2}} \tag{A1}$$

$$v_S = \left(\frac{\mu}{\rho} \right)^{\frac{1}{2}} \tag{A2}$$

where v_P and v_S are the *P* wave and *S* wave velocities, respectively. K is the effective bulk modulus, μ is the shear modulus, and ρ is the density of the medium.

If velocities are known, then the bulk and shear moduli of the medium can be estimated using

$$\mu = \rho {v_S}^2 \tag{A3}$$

$$K = \rho \left({v_P}^2 - \frac{4}{3}{v_S}^2 \right). \tag{A4}$$

The change in bulk modulus of a fluid-saturated rock caused by partial replacement of the ambient brine by CO_2 can be estimated using the following equation

$$\frac{K_{sat}}{K_{min} - K_{sat}} - \frac{K_{br}}{\phi(K_{min} - K_{br})} = \frac{K_{sat}(S_{CO_2})}{K_{min} - K_{sat}(S_{CO_2})} - \frac{K_{fl}(S_{CO_2})}{\phi(K_{min} - K_{fl}(S_{CO_2}))}, \tag{A5}$$

where ϕ is the porosity of the rock, K_{sat} is the bulk modulus of the brine-saturated rock, $K_{sat}(S_{CO_2})$ is the bulk modulus of the rock with a saturation of S_{CO_2}, K_{br} is the bulk modulus of the brine, and $K_{fl}(S_{CO_2})$ is the bulk

Table A1. Parameter Values Used to Calculate v_{CO_2} and Their Uncertainties

Parameter	Symbol	Value	Uncertainty	Units
P wave velocity	v_P	2050	±30	m s^{-1}
S wave velocity	v_S	693	±25	m s^{-1}
Mineral bulk modulus	K_{min}	36.9	±0.1	GPa
Mineral density	ρ_{min}	2650	±25	kg m^{-3}
Porosity	ϕ	0.37	±0.3	
Brine bulk modulus	K_{br}	2.31	±0.1	GPa
Brine density	ρ_{br}	1040	±20	kg m^{-3}
CO_2 bulk modulus	K_{CO_2}	88	±30	MPa
CO_2 density	ρ_{CO_2}	692	±30	kg m^{-3}

modulus of the fluid mixture of CO_2 and brine. For a given saturation of CO_2, the bulk modulus of the fluid mixture is given by

$$K_{fl}(S_{CO_2}) = \left(\frac{S_{CO_2}}{K_{CO_2}} + \frac{(1 - S_{CO_2})}{K_{br}} \right)^{-1}. \quad \text{(A6)}$$

The shear modulus is unchanged by pore fluid (i.e., $\mu_{dry} = \mu_{sat}$). The density of the partially CO_2-saturated rock is given by

$$\rho(S_{CO_2}) = (1 - \phi)\rho_{min} + \phi S_{CO_2}\rho_{CO_2} + \phi(1 - S_{CO_2})\rho_{br}. \quad \text{(A7)}$$

These values are used to find $v_P(S_{CO_2})$ for $0 \leq S_{CO_2} \leq 1$ using

$$v_P(S_{CO_2}) = \left(\frac{K_{sat}(S_{CO_2}) + \frac{4}{3}\mu}{\rho(S_{CO_2})} \right)^{\frac{1}{2}}. \quad \text{(A8)}$$

The parameter values used to estimate $v_P(S_{CO_2})$ are given in Table A1. *P* and *S* wave velocities were measured at a nearby well and their values are generally agreed. For the bulk modulus and density of the mineral phase of the sandstone, there is also broad agreement, although some uncertainty is introduced by the possible variation in mineralogy within the Utsira Formation. Porosity was measured at nearby wells and does vary throughout the Utsira Formation. However, there is a broad consensus that the average value is 0.37 [*Chadwick et al.*, 2005]. The bulk modulus of the brine is well known (E. Lindeberg, written communication, 2000). Due to the uncertainties of pressure and temperature estimates for Layer 9, values of the bulk modulus and the density for dense-phase CO_2 can vary. We use values favored by the Institut Français du Petrole based on a temperature of 29°C with a methane content of 1%. Uncertainties for all input parameters were chosen to reflect the range of estimates found in the literature. Using these values, v_{CO_2} was calculated to be 1428 ± 95 m s^{-1}.

We extended our analysis by exploring how sensitive v_{CO_2} is to each of the input parameters in turn. In Figure A1, v_{CO_2} is plotted as a function of S_{CO_2} and each input parameter is varied by ±10% (Figure A1). These results show that changes in the bulk modulus and in the density of CO_2 have little impact upon the value of v_{CO_2}. The most important parameters are v_P, ρ_{min}, ϕ, and K_{br}. Since v_P and ρ_{min} are well constrained, the largest uncertainties stem from K_{br} and from the porosity distribution within the Utsira Formation.

Acknowledgments
We thank the Sleipner License Partners (Statoil, Total E&P Norge and ExxonMobil) for access to seismic reflection data sets and for permission to publish our results. We are also grateful to Matthew Falder for technical advice. L.R.C. is partly funded by the EU PANACEA consortium. J.A.N. acknowledges support from a Royal Society University Research Fellowship. J.C.W. and R.A.C. worked with support from the BIGCCS Centre under the auspices of the Norwegian research program Centres for Environment-friendly Energy Research (FME) and publish with permission of the Executive Director, British Geological Survey (NERC). Seismic reflection data sets used in this study are listed in the references and are available on request from the Sleipner License Partners. Department of Earth Sciences contribution esc.3666.

References

Arts, R., O. Eiken, A. Chadwick, P. Zweigel, L. van der Meer, and B. Zinszner (2004), Monitoring of CO_2 injected at Sleipner using time-lapse seismic data, *Energy*, *29*(9-10), 1383–1392, doi:10.1016/j.energy.2004.03.072.

Baklid, A., R. Korbol, and G. Owren (1996), Sleipner Vest CO_2 disposal, CO_2 injection into a shallow underground aquifer, paper presented at at the SPE Annual Technical Conference and Exhibition, SPE, Denver, Colo., 6–9 Oct, doi:10.2118/36600-MS.

Benson, S. M., and D. R. Cole (2008), CO_2 sequestration in deep sedimentary formations, *Elements*, *4*(5), 325–331, doi:10.2113/gselements.4.5.325.

Bickle, M., A. Chadwick, H. E. Huppert, M. Hallworth, and S. Lyle (2007), Modelling carbon dioxide accumulation at Sleipner: Implications for underground carbon storage, *Earth Planet. Sci. Lett.*, *255*(1–2), 164–176, doi:10.1016/j.epsl.2006.12.013.

Boait, F. C., N. J. White, M. J. Bickle, R. A. Chadwick, J. A. Neufeld, and H. E. Huppert (2012), Spatial and temporal evolution of injected CO_2 at the Sleipner Field, North Sea, *J. Geophys. Res.*, *117*, B03309, doi:10.1029/2011JB008603.

Cantillo, J. (2012), Throwing a new light on time-lapse technology, metrics and 4D repeatability with SDR, *Leading Edge*, *31*(4), 405–413, doi:10.1190/tle31040405.1.

Carcione, J. M., S. Picotti, D. Gei, and G. Rossi (2006), Physics and seismic modeling for monitoring CO_2 storage, *Pure Appl. Geophys.*, *163*(1), 175–207, doi:10.1007/s00024-005-0002-1.

Cavanagh, A. (2013), Benchmark calibration and prediction of the Sleipner CO_2 plume from 2006 to 2012, *Energy Procedia*, *37*, 3529–3545, doi:10.1016/j.egypro.2013.06.246.

Chadwick, R., R. Arts, O. Eiken, G. Kirby, E. Lindeberg, and P. Zweigel (2004), 4D seismic imaging of an injected CO_2 plume at the Sleipner Field, Central North Sea, *Geol. Soc. London, Mem.*, *29*(1), 311–320, doi:10.1144/GSL.MEM.2004.029.01.29.

Chadwick, R., D. Noy, R. Arts, and O. Eiken (2009), Latest time-lapse seismic data from Sleipner yield new insights into CO_2 plume development, *Energy Procedia*, *1*(1), 2103–2110, doi:10.1016/j.egypro.2009.01.274.

Chadwick, R., G. Williams, and J. White (2016), High-resolution imaging and characterization of a CO_2 layer at the Sleipner CO_2 storage operation, North Sea using time-lapse seismics, *First Break*, *34*(February), 79–88.

Chadwick, R. A., and D. J. Noy (2015), Underground CO_2 storage: Demonstrating regulatory conformance by convergence of history-matched modeled and observed CO_2 plume behavior using Sleipner time-lapse seismics, *Greenh. Gases Sci. Tech.*, *5*(3), 305–322, doi:10.1002/ghg.1488.

Chadwick, R. A., R. Arts, and O. Eiken (2005), *4D Seismic Quantification of a Growing CO_2 Plume at Sleipner, North Sea*, vol. 6, pp. 1385–1399, Geol. Soc., London, doi:10.1144/0061385.

Chadwick, R., and D. Noy (2010), History-matching flow simulations and time-lapse seismic data from the Sleipner CO_2 plume, *Geol. Soc. London, Petrol. Geo. Conf. Ser.*, *7*, 1171–1182, doi:10.1144/0071171.

Eiken, O., I. Brevik, R. Arts, E. Lindeberg, and K. Fagervik (2000), Seismic monitoring of CO_2 injected into a marine aquifer, in *SEG International Conference 70th Annual Meeting*, pp. 181–191, Geological Society of London, Calgary, Canada.

Eiken, O., P. Ringrose, C. Hermanrud, B. Nazarian, T. A. Torp, and L. Høier (2011), Lessons learned from 14 years of CCS operations: Sleipner, In Salah and Snøhvit, *Energy Procedia*, *4*, 5541–5548, doi:10.1016/j.egypro.2011.02.541.

Furre, A.-K., and O. Eiken (2014), Dual sensor streamer technology used in Sleipner CO_2 injection monitoring, *Geophys. Prospect.*, *62*(5), 1075–1088, doi:10.1111/1365-2478.12120.

Furre, A. K., A. Kiær, and O. Eiken (2015), CO_2-induced seismic time shifts at Sleipner, *Interpretation*, *3*(3), 23–35, doi:10.1190/INT-2014-0225.1.

Ghaderi, A., and M. Landrø (2009), Estimation of thickness and velocity changes of injected carbon dioxide layers from prestack time-lapse seismic data, *Geophysics*, *74*(2), O17, doi:10.1190/1.3054659.

Hall, M. (2007), Smooth operator: Smoothing seismic interpretations and attributes, *Leading Edge*, *26*(1), 16–20, doi:10.1190/1.2431821.

Kallweit, R. S., and L. C. Wood (1982), The limits of resolution of zero-phase wavelets, *Geophysics*, *47*(7), 1035, doi:10.1190/1.1441367.

Kiær, A. F. (2015), Fitting top seal topography and CO_2 layer thickness to time-lapse seismic amplitude maps at Sleipner, *Interpretation*, *3*(2), SM47–SM55, doi:10.1190/INT-2014-0225.1.

Kragh, E., and P. Christie (2002), Seismic repeatability, normalized RMS, and predictability, *Leading Edge*, *21*(7), 640–647, doi:10.1190/1.1497316.

Mavko, G., T. Mukerji, and J. Dvorkin (2009), *The Rock Physics Handbook: Tools for Seismic Analysis of Porous Media*, Cambridge Univ. Press, Cambridge, U. K.

Neufeld, J. A., and H. E. Huppert (2009), Modelling carbon dioxide sequestration in layered strata, *J. Fluid Mech.*, *625*, 353–370, doi:10.1017/S0022112008005703.

Ryan, H. (1994), Ricker, Ormsby, Klauder, Butterworth—A choice of wavelets, *Can. Soc. Explor. Geophys. Rec.*, *19*(7), 8–9.

Rubino, J. G., D. R. Velis, and M. D. Sacchi (2011), Numerical analysis of wave-induced flow effects on seismic data: Application to monitoring of CO_2 storage at the Sleipner field, *J. Geophys. Res.*, *116*, B03306, doi:10.1029/2010JB007997.

White, J. C., G. A. Williams, and R. A. Chadwick (2013), Thin layer detectability in a growing CO_2 plume: Testing the limits of time-lapse seismic resolution, *Energy Procedia*, *37*, 4356–4365, doi:10.1016/j.egypro.2013.06.338.

Widess, M. (1973), How thin is a thin bed?, *Geophysics*, *38*(6), 1176–1180, doi:10.1190/1.1440403.

Williams, G., and A. Chadwick (2012), Quantitative seismic analysis of a thin layer of CO_2 in the Sleipner injection plume, *Geophysics*, *77*(6), R245, doi:10.1190/geo2011-0449.1.

Zhang, G., P. Lu, and C. Zhu (2014), Model predictions via history matching of CO_2 plume migration at the Sleipner Project, Norwegian North Sea, *Energy Procedia*, *63*, 3000–3011, doi:10.1016/j.egypro.2014.11.323.

Zweigel, P., R. Arts, A. E. Lothe, and E. B. G. Lindeberg (2004), Reservoir geology of the Utsira Formation at the first industrial-scale underground CO_2 storage site (Sleipner area, North Sea), *Geol. Soc. London, Spec. Publ.*, *233*(1), 165–180, doi:10.1144/GSL.SP.2004.233.01.11.